ChemPubSoc Europe

DOI: 10.1002/cssc.201501574

CHEMSUSCHEM Full Papers

Solvent-Driven Gate Opening in MOF-76-Ce: Effect on CO_2 Adsorption

Jayashree Ethiraj,[a] Francesca Bonino,*[a] Jenny G. Vitillo,[a, b] Kirill A. Lomachenko,[a, c] Carlo Lamberti,[c, d] Helge Reinsch,[e] Karl Petter Lillerud,[e] and Silvia Bordiga[a]

A cerium-based metal–organic framework with MOF-76 topology has been synthesized by a very simple and fast solvothermal method that has been tested for a one gram yield. Variable-temperature powder XRD and X-ray absorption data, analyzed by Rietveld and multiple-scattering extended X-ray absorption fine-structure methods, revealed high thermal stability and the presence of three different stable structures. X-ray absorption near-edge structure and FTIR spectroscopy probed the presence of cerium(III), which was characterized by coordinatively unsaturated sites that, however, played no major role in carbon dioxide adsorption. The material revealed excellent carbon dioxide adsorption properties: the highest gravimetric capacity of 15 wt% was observed at 1.1 bar in the case of the sample activated at 250 °C in vacuum, whereas the strongest interaction energy of 35 kJ mol^{-1} was observed for the sample activated at 150 °C. Negligible nitrogen uptake of the sample activated at 150 °C indicates that this material is a promising candidate for nitrogen/carbon dioxide separation purposes.

Introduction

Microporous metal–organic frameworks (MOFs) based on lanthanide metal ions or clusters represent a group of porous materials that possesses interesting coordination, electronic, and optical properties.[1] Porous isostructural lanthanide-based MOFs, with the composition [Ln(BTC)(H_2O)]·4.3 H_2O or Ln–BTC (Ln: Ce, Tb, and Y; BTC: 1,3,5-benzenetricarboxylate), and exhibiting a tetragonal structure were synthesized by ultrasonic irradiation at room temperature and their luminescence properties were studied.[2]

The yttrium-based MOF Y(BTC)(H_2O)·4.3 H_2O showed permanent porosity, selective gas adsorption, and good hydrogen capacity upon activation.[3]

Gustasfsson et al. developed a family of homeotypic porous lanthanide MOFs [Ln(BTC)(H_2O)]·H_2O·DMF with various metal ions (Nd, Sm, Eu, Gd, Tb, Ho, Er, and Yb).[1c] The structure was first described as coincident with MOF-76 for Tb(BTC)(H_2O)1.5(DMF).[4] The structures of the as-synthesized compounds were tetragonal with 1D channels that showed accessible lanthanide ions and exhibited high thermal stability.

By focusing attention on cerium metal ions, cerium-based Werner-type tetrahedra were employed for the size-selective luminescent detection of natural carbohydrates through the incorporation of amide groups.[5] Li and Liu succeeded in obtaining single crystals of a cerium-based BTC MOF with a well-defined 3D structure, but the synthetic procedure showed difficulties in producing the material on a gram scale.[6] Furthermore, a recent paper reported that the Ce–BTC structure collapsed after removal of the solvent guest molecules.[7]

Herein, a very simple, rapid, one-pot, solvothermal procedure is reported for the synthesis of MOF-76-Ce. This method allows easy scaling up of the material. In respect to previously published data, the material revealed improved thermal stability (up to 450 °C) and the appearance of new well-defined structures upon heating. The intermediate (partly desolvated structure) shows selective adsorption towards CO_2 over N_2, and thus, it is proposed herein for use in CO_2/N_2 separation. The fully desolvated intermediate is characterized by one of the highest CO_2 volumetric densities recorded.[8] As successfully applied to other MOFs systems,[9] the combination of several structural and spectroscopic techniques has been used to disclose the complex structure of MOF-76-Ce.

[a] Dr. J. Ethiraj, Dr. F. Bonino, Dr. J. G. Vitillo, Dr. K. A. Lomachenko, Prof. S. Bordiga
Department of Chemistry, NIS and INSTM Reference Centre
University of Turin,
Via G. Quarello 15, 10135 and Via P. Giuria 7, 10125, Turin (Italy)
E-mail: francesca.bonino@unito.it

[b] Dr. J. G. Vitillo
Dipartimento di Scienza e Alta Tecnologia
Università degli Studi dell'Insubria
Via Lucini 3, 22100-Como (Italy)

[c] Dr. K. A. Lomachenko, Prof. C. Lamberti
Southern Federal University
Zorge Street 5, 344090 Rostov-on-Don (Russia)

[d] Prof. C. Lamberti
Department of Chemistry, CrisDi Centre for Crystallography
University of Turin, Via P. Giuria 7, 10125, Turin (Italy)

[e] Dr. H. Reinsch, Prof. K. P. Lillerud
inGAP Centre of Research-Based Innovation
Department of Chemistry, University of Oslo
SemSælandsvei 26, 0315 Oslo (Norway)

Supporting Information and ORCID(s) from the author(s) for this article are available on the WWW under http://dx.doi.org/10.1002/cssc.201501574.

Results and Discussion

Structure evolution of MOF-76-Ce

MOF-76-Ce was synthesized as described in the Experimental Section. Details on the morphology, thermal stability, and vibrational features are reported in the Supporting Information (Sections S1–S3). In situ variable-temperature powder XRD (VT-PXRD) data of MOF-76-Ce (formula: $[Ce(BTC)]\cdot n H_2O\cdot m DMF$) collected in a flow of nitrogen over a temperature range of 25–600 °C are reported in Figure 1. Three distinct structural

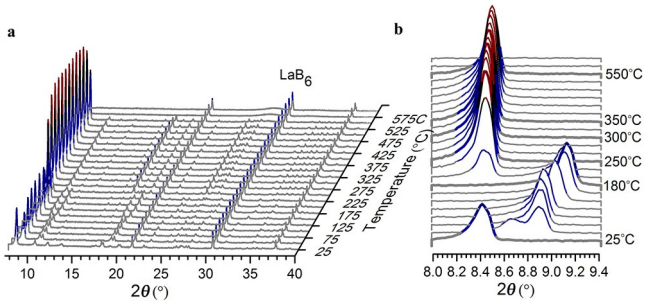

Figure 1. VT-PXRD in a flow of nitrogen showing structural changes to MOF-76-Ce during thermal treatment. a) PXRD patterns collected over a temperature range of 25–600 °C ($\lambda = 1.5418$ Å). LaB_6 is used as an internal standard (reflection at 30.39°). b) Magnification of the low-angle reflections.

modifications can be refined from the PXRD data. Starting from the as-synthesized sample (MOF-76-Ce-fs, fully solvated), the most relevant changes are observed at 180 °C (MOF-76-Ce-hs, half solvated) with a further evolution that ends at 350 °C (MOF-76-Ce-ds, desolvated). In the 250–300 °C range, the patterns do not change substantially, whereas, starting at 325 °C, the peak due to the 100, 010 reflections shifts slightly towards higher angles; this is caused by the chains of cerium atoms moving slightly closer when the flexibility of the BTC linkers increases with temperature. The connectivity of the structure is unchanged during structural changes. The transformations were found to be due to removal of water and DMF molecules from the channels in the $[Ce(BTC)]\cdot n H_2O\cdot m DMF$ structure. Similar features have been reported on single crystals of lanthanide MOFs with seven-coordinated lanthanide(III) ions linked by BTCs.[1c] At 575 °C, there is complete structural collapse with the formation of CeO_2 and coke; this is in agreement with the weight loss observed by thermogravimetric analysis (TGA; Section S2 in the Supporting Information).

Rietveld refinement of the structures was carried out by using high-resolution powder patterns recorded in a flow of nitrogen at the temperatures for which the three structures were identified: 25, 180, and 350 °C. Experimental patterns and refinement results are reported in Figure S4 and Table S1 in the Supporting Information, whereas graphical representations of the structures obtained are provided in Figure 2. The pattern measured at 25 °C showed very strong similarities with a simulated pattern of MOF-76.[1c,4] Indeed, Rietveld refinement confirmed that this compound was a cerium-based analogue of the MOF-76-structure. The final structures reported in Figure 2 were obtained after several iterated PXRD and Ce L_3 edge extended X-ray absorption fine-structure (EXAFS) refinements. First, the structure obtained as a result of initial PXRD refinement was used as a model for EXAFS fitting. Then, the best-fit local environment of cerium atoms obtained by EXAFS was implemented into the periodic model of the whole material and the PXRD refinement was run again. The resulting structure was subsequently subjected to the new EXAFS fitting procedure, and so on, until after several iterations convergence of the structural parameters was reached.[9]

The inorganic building unit is based on distorted pentagonal CeO_7 bipyramids. In these polyhedra, six oxygen atoms are part of carboxylate groups, whereas one oxygen atom belongs to a solvent molecule (water or DMF; see Figure 2, left, and Figure 3, MOF-76-Ce-fs). Each BTC linker is connected to six cerium atoms: two in one cerium chain and four on the opposite chain. Each carboxylate group bridges two cerium atoms. The orientation of the BTC linkers alternates to form regular sinusoidal chains of cerium atom (see Figure 2, left). The sheets are connected in a similar way with another set of BTC linkers orthogonal to the plane of Figure 2. This movement in and out of the plane in two directions arranges the CeO_7 units into helical chains to form 4_3-screw axes. The organic trimesate anions (BTC linkers) are situated parallel to the (100) and (010) planes, forming non-interconnected square-shaped channels. In the fully solvated structure, the channels are lined with four coordinated solvent molecules, whereas in the half solvated

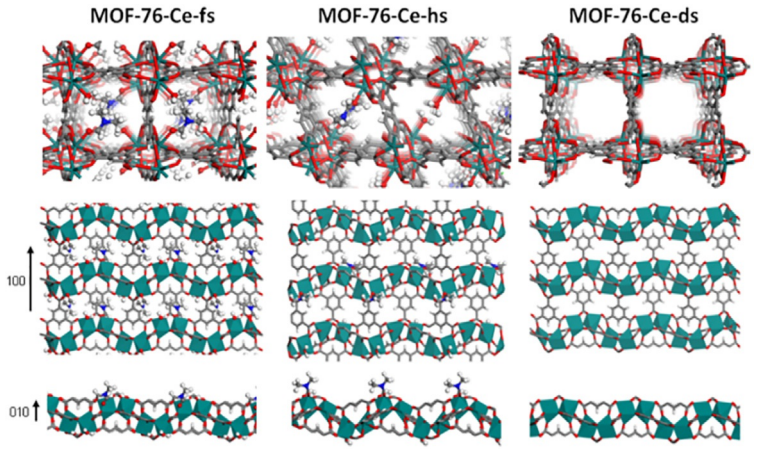

Figure 2. Structures of MOF-76-Ce. Left: MOF-76-Ce-fs; middle: MOF-76-Ce-hs; right: MOF-76-Ce-ds. Top row: tridimensional representation (view along the 001 direction) of the frameworks with sticks (solvent molecules are represented by sticks and balls). Cerium: dark cyan; oxygen: red; nitrogen: blue; carbon: gray; hydrogen: white. Middle row: layers of Ce and BTC linkers viewed along the 010 direction. Bottom row: one chain of Ce with the coordinating carboxylic groups and solvent molecules (viewed along the 100 direction). For MOF-76-Ce-fs and MOF-76-Ce-hs, DMF and water have been arbitrarily alternated into the framework. For MOF-76-Ce-fs, solvent molecules not coordinated to Ce sites have been omitted. The coordination environment at the cerium sites is illustrated by polyhedra in medium and bottom rows.

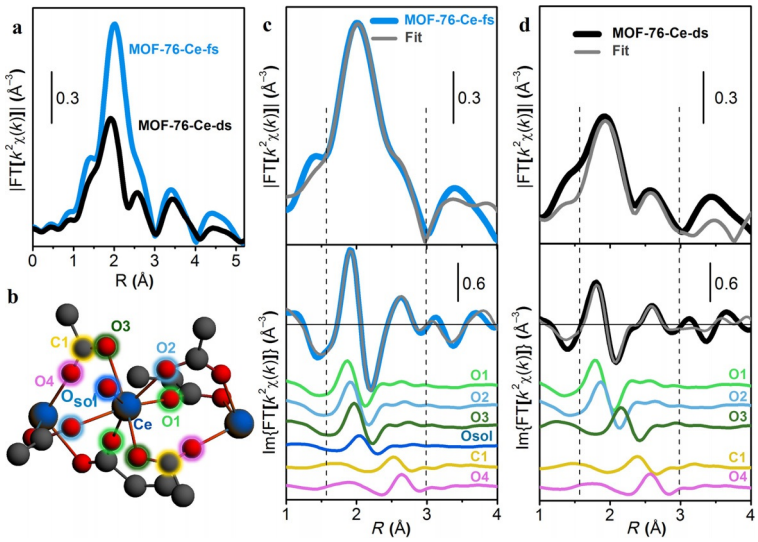

Figure 3. EXAFS analysis of MOF-76-Ce. a) Fourier-transform (FT) modulus of the experimentally obtained, phase-uncorrected, k^2-weighted Ce L_3-edge EXAFS signal of MOF-76-Ce. b) The atomic cluster used for EXAFS fitting. Cerium: blue; oxygen: red; carbon: gray. Atoms that constitute the nearest coordination of cerium and contribute most to the EXAFS signal are labeled and highlighted by colored halos. The absorbing cerium atom is in the center of the cluster. Comparison between experimental and fitted EXAFS signals for MOF-76-Ce-fs (c) and MOF-76-Ce-ds (d). The top panels show the moduli of EXAFS FT, whereas the bottom panels exhibit the imaginary parts of the FT together with the contributions of the principal scattering paths. Vertical dashed lines indicate the boundaries of the fitted region. The color of the signal for each path matches the color of the halo in b) assigned to the atoms that form the path. With exception of solvent oxygen, O_{sol}, each path is formed by the two atoms equidistant from Ce that have halos of the same color.

(180 °C) structure the solvent molecules are removed in an ordered manner (Figure 2, middle, MOF-76-Ce-hs). The distribution of solvent molecules reported in Figure 2 are arbitrarily represented. In particular, in the case of the fully solvated sample, an alternate arrangement of water and DMF molecules has been considered. For the sake of simplicity, disordered, unbonded solvent molecules have been omitted. In case of the MOF-76-Ce-hs structure (Figure 2, middle), in principle, DMF and water should both be taken into account; however, only DMF molecules fit perfectly (water would be too small) and distort the channels, and thereby, creating the structure through diagonal contraction of the channels. In this intermediate structure, the solvent molecules are removed at two opposite corners of the channels, which leads to a distortion of the angle at these corners from the ideal value of 90° in MOF-76-Ce-fs to 68° in MOF-76-Ce-hs. As a consequence, the opposite angles are expanded from 90 to 112°. Rhombic channels are therefore observed, in which the coordinated solvent molecules are present as nonconnecting pillars pointing into the pores. Notably, the partially desolvated structure (MOF-76-Ce-hs) shows major changes in the free-space topology: channels along the [001] direction are strongly bent (Figure 2, middle, bottom row) and the DMF molecules protrude much more into the channels than in case of MOF-76-Ce-fs (Figure 2, left, bottom row). When all solvents molecules are removed, the structure relaxes to a square shape similar to the one with symmetric loading of solvent molecules. (Figure 2, right, MOF-76-Ce-ds). In this framework, all coordinated solvent molecules are removed and the original symmetry is restored. The connectivity of the cerium ions involving the carboxylate groups remains unchanged. Cerium ions simply change the local symmetry from a distorted pentagonal bipyramid in MOF-76-Ce-fs to a distorted trigonal prism in MOF-76-Ce-ds.

The PXRD patterns of MOF-76-Ce-hs and MOF-76-Ce-ds were reproduced upon activation in vacuum at 150 and 250 °C (see Figure S5 in the Supporting Information); this showed that both structures were obtained under slightly different conditions if samples were treated in vacuum or in a flow of gas. Activated samples lose crystallinity if re-exposed to air.

To refine the local coordination environment of cerium, Ce L_3-edge EXAFS spectra were measured in situ during activation. Data were collected for MOF-76-Ce-fs during heating to 350 °C in a flow of helium and after subsequent cooling back to room temperature without interrupting the flow of helium (MOF-76-Ce-ds). In this way, the spectra of MOF-76-Ce-fs and MOF-76-Ce-ds were directly comparable without bias due to thermal effects.

Figure 3a shows the experimental EXAFS signals for the initial and final states of the activation process. Data indicate that the major changes upon activation happen in the nearest environment of cerium atoms (oxygen and carbon atoms within 3.5 Å from Ce that contribute to the phase-uncorrected EXAFS in the range of 1.5–3.0 Å), since the largest peak centered at 2 Å is dramatically perturbed, whereas more distant coordination shells are much less affected. The main changes upon activation happen at around 90 °C; these were monitored by mass spectrometry (see Figure S6b in the Supporting Information), which indicated that the changes coincided with the release of water. However, only the loss of one water molecule per cerium atom is not sufficient to cause such remarkable changes to the EXAFS signal. At the same time, the loss of a significantly larger fraction of coordinated first-shell ligands would not have been consistent with the crystal structure indicated by PXRD. To explain changes to the spectra, the EXAFS data were fitted by using the corresponding PXRD geometries as starting points. Figure 3b shows the cluster used for MOF-76-Ce-fs. The activated structure lacks solvent oxygen, O_{sol}, but otherwise is qualitatively similar, and therefore, is not presented for the sake of brevity. Obtained fits are in good agreement with experimental data (Figure 3c and d). In MOF-76-Ce-fs, the main peak is due to scattering from four pairs of oxygen atoms (O1–4), one pair of carbon atoms (C1), and one oxygen atom of an adsorbed solvent molecule (O_{sol}). Despite the impressive decrease in intensity of the first EXAFS peak in the activated material, it was confirmed that, upon activation until 350 °C, only the solvent molecule desorbed, while all other atoms in the nearest vicinity of cerium remained. The decrease of the main peak is explained by a severe antiphase effect due to significant elongation of the Ce–O3 distance from 2.55 to 2.75 Å. Although in the solvated material the con-

tribution from this path (dark-green curve in Figure 3c and d) is almost perfectly in phase with those of O1 and O2, in the activated form it goes exactly out of phase, which, accompanied by the loss of O_{sol}, causes the observed damping effect. Consequently, the contribution from C1 and O4 becomes visible as a separate peak at around 2.6 Å, whereas in the solvated material it is only a shoulder on the high-*R* side of the main maximum (see Tables S2 and S3 in the Supporting Information).

The oxidation state of the cerium ion in MOF-76-Ce was studied by X-ray absorption near-edge structure (XANES) and FTIR methods (Figure 4).

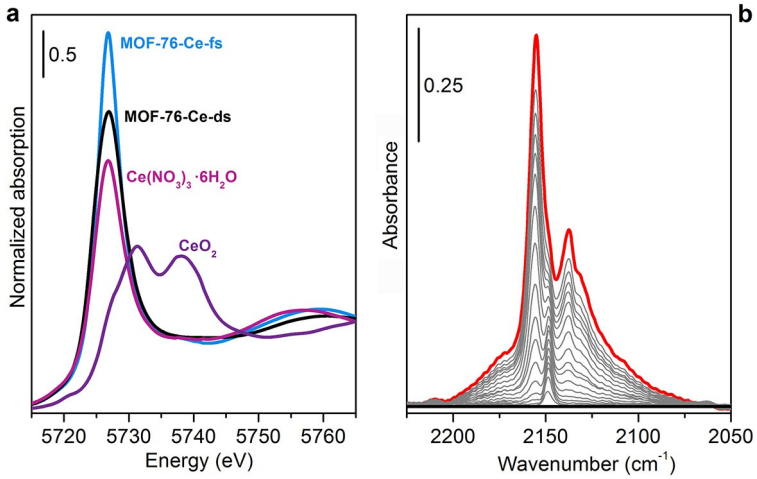

Figure 4. a) Ce L_3-edge XANES spectra of MOF-76-Ce-fs and MOF-76-Ce-ds, compared with Ce^{IV} oxide and Ce^{III} nitrate hexahydrate. All spectra have been collected at room temperature. b) FTIR spectra of CO adsorption at −196 °C for MOF-76-Ce-ds (black curve); red and gray curves represent the highest (p = 10 mbar; 1 bar = 10^5 Pa) and intermediate coverages obtained upon progressive outgassing, respectively.

Ce L_3-edge XANES spectra serve as a very reliable indicator for Ce oxidation state because the shapes of the L_3 edge for Ce^{IV} and Ce^{III} are completely different. Ce^{IV} gives rise to a double-peaked main maximum with two low-energy shoulders, whereas Ce^{III} produces a very intense single-peaked white line.[10] Typical examples that illustrate these two different cases are cerium(IV) oxide and cerium(III) nitrate, which were used in our XANES experiments as reference compounds (Figure 4a). Ce L_3-edge XANES spectra of the MOF were collected simultaneously with EXAFS data, and showed no substantial change to the Ce^{3+} oxidation state during sample treatment in an inert flow.

Trivalent cerium species, with at least one coordination vacancy, were monitored by IR spectroscopy for MOF-76-Ce-ds upon CO adsorption (Figure 4b). It is well known that the CO vibrational frequency is able to shift differently after coordination by Ce^{3+} or Ce^{4+} centers.[11] In this experiment, 10 mbar of CO were dosed at liquid nitrogen temperature on a self-supported pellet of MOF-76-Ce-ds (obtained by pretreatment in dynamic vacuo at 250 °C for 2 h). The pressure in the cell was gradually reduced with simultaneous recording of spectra. Three distinct contributions appeared at $\tilde{\nu}$ = 2155, 2149, and 2137 cm^{-1}. The band at $\tilde{\nu}$ = 2137 cm^{-1}, which was the first to be removed upon lowering the pressure, was assigned to physisorbed CO condensed in the pores. The doublet at higher frequencies ($\tilde{\nu}$ = 2155 and 2149 cm^{-1}) required more prolonged pumping to disappear, and thus, could be assigned to CO interacting with acidic sites. At higher coverage, the feature at $\tilde{\nu}$ = 2155 cm^{-1} was dominant, whereas the one at $\tilde{\nu}$ = 2149 cm^{-1} was only a shoulder. By decreasing the CO pressure, the feature at $\tilde{\nu}$ = 2155 cm^{-1} disappears more rapidly than the one at $\tilde{\nu}$ = 2149 cm^{-1}. Because the CO vibrational mode on the MOF open metal sites is intermediate between metals in oxides and metals grafted in different systems,[12] the doublet can be ascribed to adsorption on Ce^{3+} sites, since bands due to Ce^{4+} were expected at frequencies higher than $\tilde{\nu}$ = 2156 cm^{-1},[11] in agreement with XANES results (Figure 4a). The hypothesis of two different Ce^{3+} sites, characterized by different strengths and abundancies, was ruled out because it was not supported by the structure. Thus, the band at $\tilde{\nu}$ = 2155 cm^{-1} could be tentatively assigned to CO interacting with one Ce^{3+} site and the band at $\tilde{\nu}$ = 2149 cm^{-1} to CO bridged on two close Ce^{3+} sites, on the basis of reports in the literature.[13]

CO_2 and N_2 adsorption on MOF-76-Ce

The adsorption properties of MOF-76-Ce-hs and MOF-76-Ce-ds towards CO_2 were also explored. All presented data indicate that the two materials, despite their similar structural features, such as the first coordination sphere of cerium sites, are expected to behave substantially differently.

Volumetric CO_2 isotherms recorded at 25 °C in the 0–1.1 bar pressure range on MOF-76-Ce-hs and MOF-76-Ce-ds are reported in Figure 5a for both adsorption and desorption branches (full and open circles, respectively). MOF-76-Ce-hs and MOF-76-Ce-ds show comparable uptake to a pressure of 0.15 bar, whereas at higher pressure (1.1 bar) MOF-76-Ce-ds reveals a higher CO_2 storage capacity of 4 mol kg^{-1} (15 wt%).

Table 1 reports the CO_2 storage capacity for the two samples, together with the corresponding BET and Langmuir surface areas calculated from N_2 adsorption at −196 °C (see Section S8 in the Supporting Information for further details). The Langmuir surface area value measured for MOF-76-Ce-ds was quite high (999 $m^2 g^{-1}$), whereas for MOF-76-Ce-hs this value was not measurable, which indicated that the pores of the material were not accessible to N_2. Moreover, a negligible external surface area was expected from the large dimensions of the MOF crystals (>10 μm, see Figure S1 in the Supporting Information). The "channels gates" are not open for N_2 as they are for CO_2 in the case of MOF-76-Ce-hs: it is thus evident that MOF-76-Ce-hs is expected to be a suitable material for N_2/CO_2 separation purposes, whereas MOF-76-Ce-ds would be preferable for CO_2 storage. Nitrogen measurements were then repeated at 25 °C to quantify the selectivity of these materials in flows of CO_2/N_2. The N_2 isotherms are reported in Figure 5a (triangles), whereas the adsorption selectivities for a 15%

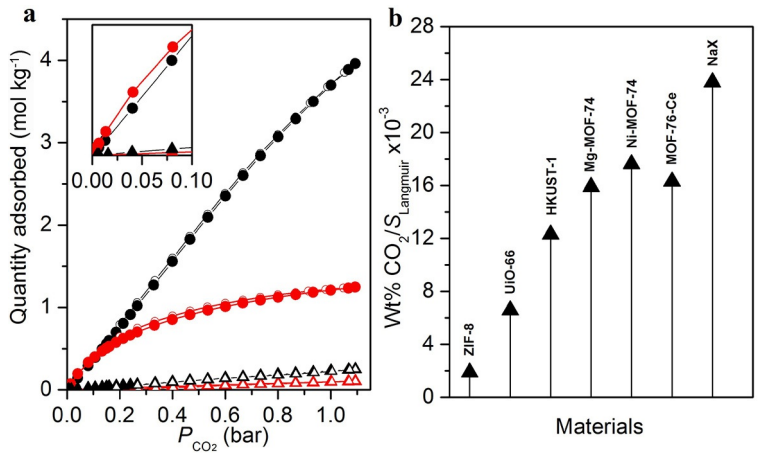

Figure 5. N_2 and CO_2 volumetric isotherms. a) Excess CO_2 and N_2 adsorption and desorption isotherms at 25 °C obtained on MOF-76-Ce-hs (red full and open circles, respectively, for CO_2, whereas triangles were adopted for N_2) and MOF-76-Ce-ds (black full and open circles, respectively, for CO_2, whereas triangles were adopted for N_2). b) Comparison of CO_2 adsorption capacities normalized to the material surface area (in m^2g^{-1}) measured at 25 °C and 1 bar for MOF-76-Ce-ds, other MOFs,[8g] and NaX.

Table 1. Surface areas, CO_2 storage capacities (at 1.1 bar and 25 °C), and differential heats of adsorption of CO_2 (q_{diff}, at 25 °C and 0.002 bar) on MOF-76-Ce. Adsorption selectivities,[a] S_{CO_2/N_2}, for a gas mixture of 15% CO_2/85% N_2 under atmospheric conditions are also reported.

MOFs	S_{BET} [m^2g^{-1}]	$S_{Langmuir}$ [m^2g^{-1}]	CO_2 amount [$mol\,kg^{-1}$]	CO_2 storage [wt%]	S_{CO_2/N_2}	q_{diff} [$kJ\,mol^{-1}$]
MOF-76-Ce-hs	n.p.[b]	n.p.[b]	1.1	4.6	33.8	35
MOF-76-Ce-ds	754	999	4.0	15	15.4	21

[a] Adsorption selectivities are defined as $S_{CO_2/N_2} = \frac{n_{CO_2} p_{N_2}}{n_{N_2} p_{CO_2}}$, in which p is the partial pressure of the gas and n is the gas adsorbed at p on the material in the corresponding pure gas isotherm. [b] n.p.: not porous.

CO_2/85% N_2 flow at 25 °C and 1 bar are reported in Table 1. These values confirmed that MOF-76-Ce-hs had a high selectivity.[8g] It is interesting that partial desolvation of the MOF structure, apart from lowering the CO_2 adsorption capacities as expected, causes an increase in the selectivity of the material. It could then be suggested the utility of retesting the best performing microporous structures reported so far in the literature for CO_2/N_2 separation at different degrees of desolvation.

For MOF-76-Ce-ds, although the amounts of CO_2 are halved with respect to those reported for the MOF with best performances under these adsorption conditions (Mg-MOF-74, 21.6 wt%),[8g] the high affinity of this material toward CO_2 can be qualitatively estimated by normalizing the CO_2 uptake to the material surface area (see Figure 5b). This results in Figure 5b suggest that MOFs with open metal sites (such as HKUST-1, Mg-MOF-74, and Ni-MOF-74) adsorb, at pressures $\leq$1 bar, more CO_2 than the other MOFs because of the positive effect of cations on the storage capacity (e.g., MOF-76-Ce-ds has a very similar performance to that of Mg-MOF-74).[8g] Moreover, when the CO_2 volumetric density (often considered to be a more important parameter for the implementation of a material in a CO_2 sequestration plant than gravimetric density)[8h] is considered, MOF-76-Ce-ds at 25 °C and 1 bar shows a value of 145 cm^3cm^{-3} at standard temperature and pressure (STP). This makes MOF-76-Ce-ds the third best performing MOF, from this point of view, and with a value close to those reported for Mg-MOF-74 (174 cm^3cm^{-3} at STP),[8h] UTSA-16 (162 cm^3cm^{-3} at STP),[8h] and NaX (177 cm^3cm^{-3} at STP).

Explanation of the CO_2 adsorption profile on MOF-76-Ce-hs is more complex and intriguing because this material has a very small accessible volume (as testified by the impossibility of measuring any surface area by N_2 adsorption at −196 °C).

For the sake of completeness, CO_2 volumetric measurements were also performed on MOF-76-Ce-ds activated at 350 and 450 °C (see Section S9 in the Supporting Information).

The affinity of CO_2 to MOF-76-Ce-hs and MOF-76-Ce-ds was further investigated by means of FTIR and microcalorimetric measurements. The FTIR adsorption results indicate that the CO_2 asymmetric stretching mode is only slightly perturbed, also for the fully desolvated sample (see Section S10 in the Supporting Information), and does not allow the two materials to be differentiated. Concerning microcalorimetry, CO_2 adsorption was measured in the pressure range of 0–0.1 bar at 30 °C (Figure 6). The isotherms are reported in Figure 6a and they clearly demonstrate a Henry-type adsorption because of the low pressure considered (only 1/10 of the Ce atoms were involved). In the first stages of adsorption, the amount of CO_2 measured reaches a value of 0.3 $mmol\,g^{-1}$ for MOF-76-Ce-hs; this is considerably higher than that for MOF-76-Ce-ds. The same trend is observed in the volumetric isotherms reported in the inset of Figure 5a. Furthermore, calorimetric data show a large difference in the initial heat of adsorption (Q^{int} in $J\,g^{-1}$) for the two materials: the value obtained for MOF-76-Ce-hs is 2.5 times that of the value obtained for MOF-76-Ce-hs (Figure 6b). At the lowest pressure, the differential adsorption heat (Figure 6c) for MOF-76-Ce-hs is nearly 35 $kJ\,mol^{-1}$; a value close to that obtained on other well-known MOFs with open metal sites, such as HKUST-1 (29 $kJ\,mol^{-1}$)[8f] and Mg-MOF-74 (39–47 $kJ\,mol^{-1}$).[8d,e] The heat of adsorption decreases to reach a plateau at 28 $kJ\,mol^{-1}$. Surprisingly, from the beginning, MOF-76-Ce-ds shows a lower interaction energy of 21 $kJ\,mol^{-1}$. This difference, in both values and evolution during increasing coverage, can be justified by the different nature of CO_2 interaction towards the surface sites. For MOF-76-Ce-hs, the significantly higher interaction energy of CO_2 could be because the CO_2 molecule has the right size to be entrapped inside the small cavities generated by the persistence of DMF molecules (see Figure 2, middle), whereas for MOF-76-Ce-ds the interaction is due to end-on $Ce^{III}\cdots CO_2$ adducts formed in the presence of a coordination vacancy at the cerium sites. Calorimetric measurements were also carried out on the material activated in vacuum at 350 °C;

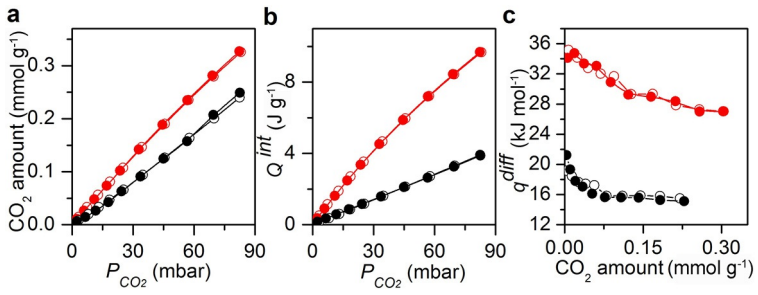

Figure 6. CO_2 microcalorimetric data. a) Volumetric CO_2 isotherms. b) Calorimetric isotherms. c) Differential heat distributions obtained on MOF-76-Ce-hs (red) and MOF-76-Ce-ds (black). Empty and full squares indicate the primary and secondary isotherms, respectively, obtained at each temperature of activation.

these results confirmed similar behavior to that obtained for MOF-76-Ce-ds (see Figure S10 in Supporting Information).

Both microcalorimetric and volumetric data show the reversibility of CO_2 adsorption at 30 and 25 °C.

Conclusions

A fast, one-pot, solvothermal synthesis for MOF-76-Ce, a material with a very high thermal stability, was optimized. Three different structures were determined by means of VT-XRD. The structures were characterized by different ratios of solvent molecules to cerium ions (1:1, 1:2, and 0). Cerium had a 3+ oxidation state and exhibited one coordination vacancy per metal center when the MOF was fully activated.

Volumetric CO_2 adsorption isotherms showed the highest value of 15 wt% at 1.1 bar for the sample activated at 250 °C. However, microcalorimetry revealed, in the lowest pressure range, the strongest interaction energy of 35 kJ mol^{-1} for the sample activated at 150 °C. The material activated at 150 °C was not accessible to N_2, whereas CO_2 strongly bonded at 30 °C. This observation could become of extreme relevance in developing this material for post-combustion CO_2 capture, also thanks to its easy synthetic procedure.

The cyclability of MOF-76-Ce upon multiple adsorption–desorption cycles will be investigated in future studies.

Experimental Section

MOF-76-Ce (as-synthesized composition [Ce(BTC)]·*n* H_2O·*m* DMF) was synthesized by using an exact amount of trimesic acid (H_3BTC 95%, Sigma Aldrich, 0.525 g, 2.5 mmol) dissolved in a mixture of DMF (Sigma Aldrich, anhydrous, 99.8%, 100 mL) and Millipore distilled water (50 mL). Then an exact amount of $Ce(NO_3)_3$·6 H_2O (Sigma Aldrich, 99.99%, 2.171 g, 5 mmol) was added to the mixture, which was stirred for 15 min and placed in a 250 mL DrySyn heating block set at 140 °C for 30 min. The precipitate was filtered, dried at 50 °C for 2 h, and washed with DMF (30 mL). The final yield was 1 g.

The PXRD patterns were collected with an X'Pert PRO MPD diffractometer from PANalytical working in Bragg–Brentano geometry by using a ceramic tube with a Cu anode as the source. Scattered photons were collected by an X'celerator detector equipped with a Ni filter to attenuate K_β. A nonambient chamber Anton Paar XRK900 instrument with Be windows was used to collect XRPD patterns as a function of temperature, in a flow of N_2 (flow rate 20 mL min^{-1}). The temperature program was set to measure the sample every 25 °C, waiting at each step for 25 min before collecting the diffractogram. The sample was heated at a heating rate of 2 °C min^{-1}. The measured temperature of the experimental chamber was subject to an error of within 5 °C. The sample was mixed with 20 wt% LaB_6 (NIST 660a standard) as a reference for both peak position and sample stage height.

High-resolution (HR) PXRD data were collected on a Bruker D8 Advance diffractometer with a LynxEye XE detector in capillary transmission mode. The radiation was $Cu_{K\alpha-1}$ selected by a Ge (111) monochromator. The sample was packed in an open 0.5 mm internal diameter quartz capillary between plugs of quartz wool and mounted in a Norby flow cell[14] and heated with a Leister LE mini hot air blower. The experiment was carried out under a constant flow of nitrogen (10 mL min^{-1}, 99.99%, AGA). An initial structural change occurred when a flow of N_2 was applied at 25 °C. The sample was heated to 180 °C at a rate of 2 °C min^{-1} with rapid data collection. The sample was then held at 180 °C and a series of patterns were collected with a count time of 1 s per step and a step size of 0.014°, until the structure stabilized. The sample was then heated to 350 °C at the same rate. A pattern was collected at 350 °C with a count time of 1 s per step and a step size of 0.014°.

All processing of the PXRD data was carried out with TOPAS. The structural transformation for the intermediate was carried out with PowderCell, and force-field calculations were performed with Materials Studio by using the universal force field (UFF).

X-ray absorption spectra at the Ce L_3 edge (5723 eV) were collected at the BM23 beamline of the European Synchrotron Radiation Facility (ESRF). The storage ring current was between 200 and 150 mA. Incident radiation was subject to harmonic rejection by a Si mirror and monochromatized by a double-crystal Si (111) monochromator. Data were acquired up to the Ce L_2 edge (6164 eV), which limited the EXAFS signal down to $k \approx 10$ Å^{-1}. The acquisition step was set to 0.3 eV in the near-edge region and $\Delta k = 0.035$ Å^{-1} in the EXAFS part of the spectrum. We used three He/N_2-filled ionization chambers as I_0, I_1 and I_2 detectors, placing chromium foil between I_1 and I_2 for energy calibration. The acquisition time was set to 1 s per point in the XANES region and then increased quadratically to 2 s per point at the end of the spectrum. XANES and EXAFS data were analyzed by using the Demeter 0.9.20 package.[15] Sample treatment was carried out in an in situ cell under a flow of helium (80 mL min^{-1}). During activation, the sample was heated to 350 °C at a ramp rate of 4 °C min^{-1} and then cooled to 30 °C.

FTIR spectra were collected on a Nicolet-6700 spectrometer equipped with a MCT B type detector, in the range of $\tilde{\nu} = 4000$–400 cm^{-1}, in transmission mode with a resolution of 2 cm^{-1}, as an average of 64 scans.

N_2 and CO_2 adsorption isotherms were collected at 25 °C on a volumetric instrument (Micromeritics ASAP 2020 sorption analyzer) by using an isothermal water bath at 25 °C.

N_2 adsorption isotherms were also collected at −196 °C for surface area evaluations.

Before each volumetric measurement, the samples (> 200 mg) were activated under vacuum at 150, 250, 350, and 450 °C on the

same vacuum equipment as that used for FTIR measurements. The samples were transferred to the measurement cell in a MBraun Star glove box (H_2O, $O_2 < 0.5$ ppm).

The heat of adsorption and adsorption isotherms were measured simultaneously by means of a C80 microcalorimeter (Calvet type, Setaram, France) at 30 °C (a well-established stepwise procedure is described in the Supporting Information and Ref. [16]). Before each calorimetric measurement, the samples were activated under vacuum at different temperatures. After the first adsorption run, the samples were outgassed at 30 °C overnight in the calorimeter before the second adsorption run was performed, so that the non-desorbable (irreversible) adsorbed fraction could be determined.

Acknowledgements

MIUR-PRIN 2010-2011 (project no. 2010A2FSS9) is kindly acknowledged for financial support. K.A.L. and C.L. acknowledge funding from the Mega-grant of the Russian Federation Government to support scientific research at SFedU (no. 14.Y26.31.0001). We acknowledge the use of the Norwegian national infrastructure for X-ray diffraction and scattering (RECX), Norwegian Research Council project 208896. Cesare Atzori, a master's student, is kindly acknowledged for his help in performing some of the experiments. Dr. Alberto Castellero and Dr. Gianluca Fiore are acknowledged for help with VT-XRD measurements.

Keywords: adsorption · carbon dioxide capture · cerium · metal–organic frameworks · X-ray diffraction

[1] a) Y. Chen, S. Q. Ma, *Rev. Inorg. Chem.* **2012**, *32*, 81 – 100; b) L. D'Arras, C. Sassoye, L. Rozes, C. Sanchez, J. Marrot, S. Marree, C. Aymonier, *New J. Chem.* **2014**, *38*, 1477 – 1483; c) M. Gustafsson, A. Bartoszewicz, B. Martin-Matute, J. L. Sun, J. Grins, T. Zhao, Z. Y. Li, G. S. Zhu, X. D. Zou, *Chem. Mater.* **2010**, *22*, 3316 – 3322.

[2] N. A. Khan, M. M. Haque, S. H. Jhung, *Eur. J. Inorg. Chem.* **2010**, 4975 – 4981.

[3] J. H. Luo, H. W. Xu, Y. Liu, Y. S. Zhao, L. L. Daemen, C. Brown, T. V. Timofeeva, S. Q. Ma, H. C. Zhou, *J. Am. Chem. Soc.* **2008**, *130*, 9626 – 9627.

[4] N. L. Rosi, J. Kim, M. Eddaoudi, B. L. Chen, M. O'Keeffe, O. M. Yaghi, *J. Am. Chem. Soc.* **2005**, *127*, 1504 – 1518.

[5] Y. Liu, X. Wu, C. He, Y. Jiao, C. Y. Duan, *Chem. Commun.* **2009**, 7554 – 7556.

[6] Z. Li, K. Liu, *Acta Crystallogr. Sect. E* **2011**, *67*, m1020.

[7] M. Almáši, V. Zeleňáka, M. Opanasenkob, I. Císařovác, *Catal. Today* **2015**, *243*, 184 – 194.

[8] a) Z. Zhang, Z.-Z. Yao, S. Xiang, B. Chen, *Energy Environ. Sci.* **2014**, *7*, 2868 – 2899; b) O. Shekhah, Y. Belmabkhout, Z. Chen, V. Guillerm, A. Cairns, K. Adil, M. Eddaoudi, *Nat. Commun.* **2014**, *5*, 4228; c) P. Nugent, Y. Belmabkhout, S. D. Burd, A. J. Cairns, R. Luebke, K. Forrest, T. Pham, S. Ma, B. Space, L. Wojtas, M. Eddaoudi, M. J. Zaworotko, *Nature* **2013**, *495*, 80 – 84; d) D. Britt, H. Furukawa, B. Wang, T. G. Glover, O. M. Yaghi, *Proc. Natl. Acad. Sci. USA* **2009**, *106*, 20637 – 20640; e) S. R. Caskey, A. G. Wong-Foy, A. J. Matzger, *J. Am. Chem. Soc.* **2008**, *130*, 10870 – 10871; f) L. Grajciar, A. D. Wiersum, P. L. Llewellyn, J. S. Chang, P. Nachtigall, *J. Phys. Chem. C* **2011**, *115*, 17925 – 17933; g) K. Sumida, D. L. Rogow, J. A. Mason, T. M. McDonald, E. D. Bloch, Z. R. Herm, T.-H. Bae, J. R. Long, *Chem. Rev.* **2012**, *112*, 724 – 781; h) S. C. Xiang, Y. B. He, Z. J. Zhang, H. Wu, W. Zhou, R. Krishna, B. L. Chen, *Nat. Commun.* **2012**, *3*, 954; i) J. G. Vitillo, *RSC Adv.* **2015**, *5*, 36192 – 36239.

[9] a) L. Valenzano, B. Civalleri, S. Chavan, S. Bordiga, M. H. Nilsen, S. Jakobsen, K. P. Lillerud, C. Lamberti, *Chem. Mater.* **2011**, *23*, 1700 – 1718; b) S. Bordiga, F. Bonino, K. P. Lillerud, C. Lamberti, *Chem. Soc. Rev.* **2010**, *39*, 4885 – 4927; c) J. H. Cavka, S. Jakobsen, U. Olsbye, N. Guillou, C. Lamberti, S. Bordiga, K. P. Lillerud, *J. Am. Chem. Soc.* **2008**, *130*, 13850 – 13851; d) F. Bonino, S. Chavan, J. G. Vitillo, E. Groppo, G. Agostini, C. Lamberti, P. D. C. Dietzel, C. Prestipino, S. Bordiga, *Chem. Mater.* **2008**, *20*, 4957 – 4968; e) J. Hafizovic, M. Bjorgen, U. Olsbye, P. D. C. Dietzel, S. Bordiga, C. Prestipino, C. Lamberti, K. P. Lillerud, *J. Am. Chem. Soc.* **2007**, *129*, 3612 – 3620; f) C. Prestipino, L. Regli, J. G. Vitillo, F. Bonino, A. Damin, C. Lamberti, A. Zecchina, P. L. Solari, K. O. Kongshaug, S. Bordiga, *Chem. Mater.* **2006**, *18*, 1337 – 1346.

[10] a) L. Barrio, G. Zhou, I. D. Gonzalez, M. Estrella, J. Hanson, J. A. Rodriguez, R. M. Navarro, J. L. G. Fierro, *Phys. Chem. Chem. Phys.* **2012**, *14*, 2192 – 2202; b) J. El Fallah, S. Boujana, H. Dexpert, A. Kiennemann, J. Majerus, O. Touret, F. Villain, F. Lenormand, *J. Phys. Chem.* **1994**, *98*, 5522 – 5533; c) G. Jacobs, P. M. Patterson, L. Williams, E. Chenu, D. Sparks, G. Thomas, B. H. Davis, *Appl. Catal. A* **2004**, *262*, 177 – 187; d) S. H. Overbury, D. R. Huntley, D. R. Mullins, G. N. Glavee, *Catal. Lett.* **1998**, *51*, 133 – 138; e) A. V. Soldatov, T. S. Ivanchenko, S. Della Longa, A. Kotani, Y. Iwamoto, A. Bianconi, *Phys. Rev. B* **1994**, *50*, 5074 – 5080.

[11] a) F. Vindigni, M. Manzoli, T. Tabakova, V. Idakiev, F. Boccuzzi, A. Chiorino, *Phys. Chem. Chem. Phys.* **2013**, *15*, 13400 – 13408; b) C. Binet, M. Daturi, J. C. Lavalley, *Catal. Today* **1999**, *50*, 207 – 225.

[12] a) S. Chavan, F. Bonino, J. G. Vitillo, E. Groppo, C. Lamberti, P. D. C. Dietzel, A. Zecchina, S. Bordiga, *Phys. Chem. Chem. Phys.* **2009**, *11*, 9811 – 9822; b) S. Bordiga, L. Regli, F. Bonino, E. Groppo, C. Lamberti, B. Xiao, P. S. Wheatley, R. E. Morris, A. Zecchina, *Phys. Chem. Chem. Phys.* **2007**, *9*, 2676 – 2685.

[13] E. Garrone, R. Bulanek, K. Frolich, C. O. Arean, M. R. Delgado, G. T. Palomino, D. Nachtigallova, P. Nachtigall, *J. Phys. Chem. B* **2006**, *110*, 22542 – 22550.

[14] P. Norby, *Mater. Sci. Forum* **1996**, *228 – 231*, 147 – 152.

[15] B. Ravel, M. Newville, *J. Synchrotron Radiat.* **2005**, *12*, 537 – 541.

[16] a) V. Bolis in *Calorimetry and Thermal Methods in Catalysis, Vol. 154* (Ed.: A. Auroux), Springer, Heidelberg, **2013**, pp. 3 – 50; b) V. Bolis, S. Maggiorini, L. Meda, F. D'Acapito, G. Turnes Palomino, S. Bordiga, C. Lamberti, *J. Chem. Phys.* **2000**, *113*, 9248 – 9261.

Received: November 24, 2015
Published online on February 19, 2016